Cold phase fluid model of the longitudinal dynamics of space-charge-dominated beams

Michiel J. L. de Hoon[a] and Edward P. Lee
Ernest Orlando Lawrence Berkeley National Laboratory, MS 47-112, One Cyclotron Road, Berkeley, California 94720

John J. Barnard and Alex Friedman
Lawrence Livermore National Laboratory, MS L-645, 7000 East Avenue, Livermore, California 94550

(Received 3 April 2002; accepted 27 November 2002)

The dynamics of a longitudinally cold, charged-particle beam can be simulated by dividing the beam into slices and calculating the motion of the slice boundaries due to the longitudinal electric field generated by the beam. On each time step, the beam charge is deposited onto an (r, z) grid, and an existing (r, z) electrostatic field solver is used to find the longitudinal electric field. Transversely, the beam envelope equation is used for each slice boundary separately. In contrast to the g-factor model, it can be shown analytically that the repulsive electric field of a slice compressed to zero length is bounded. Consequently, this model allows slices to overtake their neighbors, effectively incorporating mixing. The model then effectively describes a cold fluid in longitudinal z, v_z phase space. Longitudinal beam compression calculations based on this cold phase fluid model showed that slice overtaking reflects local mixing, while the global phase space structure is preserved. © *2003 American Institute of Physics.* [DOI: 10.1063/1.1541015]

I. INTRODUCTION

Charged-particle beams can be compressed longitudinally by imposing a head-to-tail velocity gradient. The transverse focusing lattice in which compression takes place should be designed carefully to ensure that the beam remain approximately matched. In order to design such a lattice, the longitudinal dynamics of the beam needs to be simulated accurately, such that the longitudinal compression and therefore the beam current at a given location along the lattice can be calculated correctly.

Generally, three-dimensional (3D) particle-in-cell simulations take a large amount of computing time and are therefore unattractive as design and scoping tools. Instead, a longitudinal fluid/transverse envelope model as shown in Fig. 1 can be used.[1] In this model, the beam is divided into slices longitudinally. In the nonrelativistic limit, the longitudinal beam dynamics can then be calculated by solving Newton's equation for each slice boundary separately:

$$m\frac{\mathrm{d}v_i}{\mathrm{d}t} = qeE_z(z_i), \tag{1}$$

in which m and qe are the particle mass and charge, z_i and v_i are the longitudinal position and velocity of slice boundary i, and E_z is the longitudinal electric field generated by the beam.

In addition to the longitudinal position and velocity, a horizontal and vertical beam semi-axis is associated with each slice boundary. The transverse dynamics of the beam are then calculated by employing the transverse envelope equation for each slice boundary separately. Since the shielding of the longitudinal electric field by the conducting pipe surrounding the beam depends on the distance of the beam to the pipe wall, an accurate calculation of the transverse beam dynamics is necessary to simulate the longitudinal dynamics correctly.

The longitudinal electric field E_z can be calculated in several ways. Most commonly, the g-factor model is used:[2]

$$E_z = -\frac{g}{4\pi\epsilon_0}\frac{\partial\lambda}{\partial z}, \tag{2}$$

in which λ is the line charge density and g is a geometry factor given by

$$g = \ln\left(\frac{R^2}{a_\mathrm{h}a_\mathrm{v}}\right), \tag{3}$$

in which R is the pipe radius and a_h and a_v are the horizontal and vertical beam semi-axes. The g-factor model is valid if the beam density ρ is uniform, and the beam semi-axes as well as the line charge density vary slowly over a longitudinal distance comparable to the pipe radius.

The g-factor model applied to an ideal cold fluid breaks down in three cases. Near the beam ends, the beam semi-axes and line charge density vary rapidly, thereby violating the assumptions of the g-factor model. Second, for highly compressed beams, the beam length may be short or comparable to the pipe radius. Finally, in shocks the beam properties vary rapidly over a short distance.

More accurate variants of the g-factor model have been derived, in which the restrictions on the validity of the g-factor model are eased.[3] Using these models, it was noticed in simulations that slices tend to overtake each other, particularly near the beam ends if a large ($\gtrsim 100$) number of

[a]Present address: Human Genome Center, Institute of Medical Science, University of Tokyo, Japan; electronic mail: mdehoon@ims.u-tokyo.ac.jp

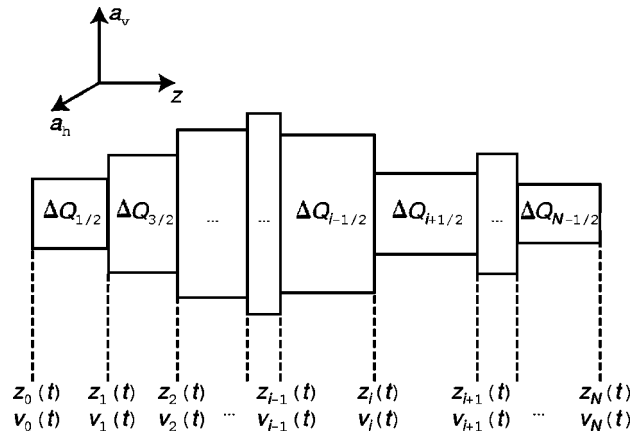

FIG. 1. The longitudinal fluid/transverse envelope model.

slices were used. This produced unphysical results, since the charge of a slice compressed to zero width leads to an infinitely large current at that location.

Previously, several explanations for the occurrence of slice overtaking have been proposed.[4,5] First, the fluid model may be invalid in the physical regime of interest. Second, the nonlinear nature of the fluid equations may cause longitudinal acoustic waves occurring in the beam to steepen into shock waves. The fluid model then breaks down as fluid properties become double-valued. Finally, the calculated longitudinal electric field may be insufficiently accurate, particularly near the beam ends.

In this paper, we will derive an analytic expression for the longitudinal electric field in a charged-particle beam. From this expression, we can show that the model shown in Fig. 1 allows slice overtaking to occur. This means that a conventional fluid model breaks down. Next, we describe a new method to calculate the space charge field by depositing the charge of the beam onto an (r, z) grid and using an existing (r, z) field solver to find the longitudinal electric field. This method should give accurate results, even in the regimes where the g-factor model fails. We then allow slices in the model to pass through each other, resulting in a cold phase fluid model, in which the beam is described as a cold fluid in z, v_z phase space.

II. THE LONGITUDINAL FIELD OF A SPACE-CHARGE-DOMINATED BEAM

First, we derive analytically the longitudinal electric field of a beam in an infinitely long circular pipe. At beam energies relevant to heavy-ion inertial fusion, the beam can be considered to be nonrelativistic in the beam frame. By solving the equations of motion in the classical limit in the beam frame, followed by a transformation to the laboratory frame, relativistic effects can be captured to first order. We will therefore calculate the longitudinal field generated by the beam in the beam frame in the nonrelativistic limit.

We approximate the beam to be circular transversely instead of elliptical, using $a=\sqrt{a_h a_v}$ for the radius. Poisson's equation can then be written as

$$\frac{1}{r}\frac{\partial}{\partial r}\left(r\frac{\partial\phi}{\partial r}\right)+\frac{\partial^2\phi}{\partial z^2}=-\frac{\rho}{\epsilon_0}. \tag{4}$$

The solution to this equation can be written in terms of a Fourier–Bessel expansion:

$$\phi(r,z)=\sum_{n=1}^{\infty} f_n(z)J_0\left(\frac{x_n r}{R}\right), \tag{5}$$

in which J_0 is the Bessel function of order zero, x_n is the nth zero of J_0, and $f_n(z)$ is a set of functions to be determined. We assume that the charge density is transversely uniform up to the beam radius $a(z)$:

$$\rho(r,z)=\frac{\lambda(z)}{\pi a(z)^2}\theta\left(1-\frac{r}{a(z)}\right), \tag{6}$$

in which λ is the line charge density and θ is the Heaviside step function. For different values of n, the Bessel functions $J_0(x_n r/R)$ are orthogonal.[6] We can then find an ordinary differential equation for $f_n(z)$:

$$f_n''(z)-f_n(z)\left(\frac{x_n}{R}\right)^2 = -\frac{2}{\epsilon_0}\frac{\lambda(z)}{\pi a(z)}\frac{1}{[x_n J_1(x_n)]^2}\frac{x_n}{R}J_1\left(\frac{x_n a(z)}{R}\right), \tag{7}$$

in which the primes denote differentiation with respect to z. This equation can be solved as[3]

$$f_n(z)=\frac{1}{\pi\epsilon_0}\frac{1}{[x_n J_1(x_n)]^2} \times\int_{-\infty}^{\infty}\exp\left(-\frac{x_n}{R}|z-z'|\right)J_1\left(\frac{x_n a(z')}{R}\right)\frac{\lambda(z')}{a(z')}dz', \tag{8}$$

in which we used the boundary condition that $f_n(z)\to 0$ for $|z|\to\infty$. Summing over the Fourier–Bessel components then gives

$$\phi(r,z)=\frac{1}{\pi\epsilon_0}\sum_{n=1}^{\infty}J_0\left(\frac{x_n r}{R}\right)\frac{1}{[x_n J_1(x_n)]^2} \times\int_{-\infty}^{\infty}\exp\left(-\frac{x_n}{R}|z-z'|\right)J_1\left(\frac{x_n a(z')}{R}\right)\frac{\lambda(z')}{a(z')}dz'. \tag{9}$$

To find the longitudinal electric field, we take the partial derivative with respect to z and average transversely:

$$\langle E_z(z)\rangle=-\frac{1}{\pi a^2}\int_0^a\frac{\partial\phi(r,z)}{\partial z}2\pi r\,dr. \tag{10}$$

This yields

$$\langle E_z(z)\rangle=\frac{2}{\pi\epsilon_0 a(z)}\sum_{n=1}^{\infty}\frac{1}{[x_n J_1(x_n)]^2}J_1\left(\frac{x_n a(z)}{R}\right) \times\int_{-\infty}^{\infty}\mathrm{sgn}(z-z')\exp\left(-\frac{x_n}{R}|z-z'|\right) \cdot\left\{J_1\left(\frac{x_n a(z')}{R}\right)\frac{\lambda(z')}{a(z')}\right\}dz'. \tag{11}$$

Incidentally, we can derive the g-factor model from this equation by assuming that the charge density $\lambda/\pi a^2$ is uniform throughout the beam and expanding the factor in brackets in a Taylor-series around $z'=z$:

$$\langle E_z(z)\rangle = -\frac{2}{\pi\epsilon_0}\frac{\partial\lambda(z)}{\partial z} \times\sum_{n=1}^{\infty}\frac{R}{x_n a}\frac{1}{[x_n J_1(x_n)]^2}J_1\left(\frac{x_n a}{R}\right)J_0\left(\frac{x_n a}{R}\right). \tag{12}$$

Using Eq. (A3) in the Appendix, we can evaluate the sum as $\frac{1}{4}\ln(R/a)$ to find the g-factor model given in Eqs. (2), (3).

Now we can calculate the longitudinal electric field acting on a slice boundary for a single slice of length $2L$ with uniform line charge density λ and beam radius a. In Eq. (11), we use $\lambda(z')=\lambda[\theta(z'-L)-\theta(z'+L)]$ and $a(z')=a$ to find

$$\langle E_z(z)\rangle = \frac{2\lambda}{\pi\epsilon_0 a^2}\sum_{n=1}^{\infty}\left[\frac{J_1\left(\frac{x_n a}{R}\right)}{x_n J_1(x_n)}\right]^2\frac{R}{x_n} \times 2\exp\left(-\frac{x_n L}{R}\right)\sinh\left(\frac{x_n z}{R}\right). \tag{13}$$

On the slice boundaries, $z=\pm L$, we find

$$\langle E_z(\pm L)\rangle = \pm\frac{2\lambda}{\pi\epsilon_0 a^2}\sum_{n=1}^{\infty}\left[\frac{J_1\left(\frac{x_n a}{R}\right)}{x_n J_1(x_n)}\right]^2\frac{R}{x_n} \times\left[1-\exp\left(-\frac{2x_n L}{R}\right)\right]. \tag{14}$$

For a slice compressed to zero length ($L\to 0$), this gives

$$\langle E_z\rangle_{\pm} = \pm\frac{4\lambda L}{\pi\epsilon_0 a^2}\sum_{n=1}^{\infty}\left[\frac{J_1\left(\frac{x_n a}{R}\right)}{x_n J_1(x_n)}\right]^2. \tag{15}$$

The sum on the right-hand side is equal to $\frac{1}{4}$, independent of the ratio a/R, as shown in the Appendix [Eq. (A4)]. Using $2L\lambda=Q$, in which Q is the charge in the slice, we find

$$\langle E_z\rangle_{\pm} = \pm\frac{Q}{2\pi\epsilon_0 a^2}. \tag{16}$$

This equation shows that the repulsive electric field is equal to the field of an infinite slab of surface charge density $Q/\pi a^2$, as expected from Gauss' law. The repulsive electric field is finite for a nonzero beam radius a. Consequently, if two slice boundaries approach each other with a sufficiently large velocity, they will overtake each other. In comparison, in the g-factor model in Eq. (3) the derivative $\partial\lambda/\partial z$ would become infinite, yielding an unbounded repulsive force between the slice boundaries that would prevent slice overtaking.

III. THE COLD PHASE FLUID MODEL

We will now describe the cold phase fluid model, in which the longitudinal electric field is calculated accurately and slices are allowed to overtake each other. The slice boundaries are kept unbent by averaging the longitudinal electric field transversely. This model was implemented as a new module, named Hermes, of the WARP simulation package.[7] In order to calculate the longitudinal electric field accurately, WARP's (r, z) field solver was used instead of the g-factor model. The charge of the beam slices is deposited onto an (r, z) grid, assuming that transversely all slices are circular instead of elliptical, and the field solver is called to calculate the electric field. This allows us to calculate the electric field correctly even near the beam ends, and also for highly compressed beams. In addition, the field can be calculated even after slice overtaking has occurred.

In conventional fluid models, the line charge density can be calculated by expanding $Q(z)$ in a Taylor series, where $Q(z)$ is defined as the amount of charge to the left of position z. Using the variables shown in Fig. 1, we find

$$\lambda(z_i) = \left(\frac{\Delta Q_{i+1/2}}{z_{i+1}-z_i}\right)\left(\frac{z_i-z_{i-1}}{z_{i+1}-z_{i-1}}\right) + \left(\frac{\Delta Q_{i-1/2}}{z_i-z_{i-1}}\right)\left(\frac{z_{i+1}-z_i}{z_{i+1}-z_{i-1}}\right)+O(2), \tag{17}$$

which is a weighted average of the average line charge density in the two slices. If either of the slices is compressed to zero width, $\lambda(z_i)$ diverges. The current, as needed in the envelope equation, would then become infinite.

Instead, in the cold phase fluid model the line charge density is calculated by summing the charge deposited onto the (r, z) grid at a given z-location. This forces the line charge density to be finite, even in the event of slice overtaking. Effectively, the line charge density is averaged over a longitudinal distance corresponding to one grid cell width. This is similar to the concept of artificial viscosity,[8,9] where a steep gradient is artificially smeared over several grid cell widths in order to avoid divergences.

Alternatively, one may consider expanding the inverse function $z(Q)$, which yields

$$\frac{1}{\lambda(z_i)} = \left(\frac{z_{i+1}-z_i}{\Delta Q_{i+1/2}}\right)\left(\frac{\Delta Q_{i-1/2}}{\Delta Q_{i+1/2}+\Delta Q_{i-1/2}}\right) + \left(\frac{z_i-z_{i-1}}{\Delta Q_{i-1/2}}\right)\left(\frac{\Delta Q_{i+1/2}}{\Delta Q_{i+1/2}+\Delta Q_{i-1/2}}\right)+O(2), \tag{18}$$

which is a weighted harmonic average of the line charge density in the two slices. The line charge density calculated from this expression remains finite even if one of the two slices is compressed to zero width. If equal charges are assigned to all slices, we find

$$\lambda(z_i) = \frac{2\Delta Q}{z_{i+1}-z_{i-1}}+O(2), \tag{19}$$

which is the total charge in the two slices divided by their combined length.

The longitudinal dynamics of the beam can most easily be understood as the motion of a cold phase fluid in z, v_z phase space. The phase fluid is represented as a continuous curve in phase space. Because the curve has zero width, the phase fluid is considered to be cold. However, since we allow slice overtaking to occur in this model, the curve may fold over in phase space, which means that more than one fluid velocity may be associated with a given location z. In the limit of extreme overtaking, the resulting curve in phase space may be seen to represent in an approximate manner a thermal distribution in v_z. In most cases, however, slice overtaking is observed to occur on a much smaller scale, indicative of mixing on a micro-scale. These cases cannot be treated by a conventional fluid model, in which the current would have become infinitely large during the event of slice overtaking, causing the transverse envelope equation to break down.

The cold phase fluid model bears some similarities to a particle-in-cell model. The main differences are the connectivity between the slice boundaries and the ability of slices to stretch and contract longitudinally and transversely. In a conventional particle-in-cell simulation, particles are not ordered and have a fixed size.

IV. EXAMPLE CALCULATION

We have applied the cold phase fluid model to design an example drift compression system of the Integrated Research Experiment (IRE), a major next step in the development of Heavy Ion Inertial Fusion.[11] To design such a system, we first define a desired final pulse shape at the end of drift compression. We transport this beam backward in time over one half period of a transport lattice. As the beam expands longitudinally during this run, its current decreases, and we adjust the lattice half period and quadrupole strength to match the new current. We then reload the beam at the end of drift compression, and run it through the adjusted lattice half period. This process is iterated over until the properties of the half period have converged. We then continue to the next lattice half period. All lattice half periods are set up using this routine, until the current at the beam center has decreased to a user-specified value at the beginning of drift compression. This procedure sets up the transverse focusing lattice, and also finds the required initial beam profile and head-to-tail velocity gradient.[10]

The beam current changes most rapidly near the end of drift compression, causing a mismatch to occur there. In the backward calculation, this mismatch then persists until the beginning of drift compression. To minimize the occurrence of mismatches, the beam can be rematched at the beginning of drift compression. Since the beam current changes slowly compared to a betatron period for most of the drift compression, after rematching the beam stays adiabatically matched in a forward run. Near the end of drift compression, the rapidly increasing current again incites a mismatch. This mismatch does not affect the beam as seriously though, because it lasts for only a short distance.

Rematching the beam at the beginning of drift compression causes the forward run to differ from the backward run.

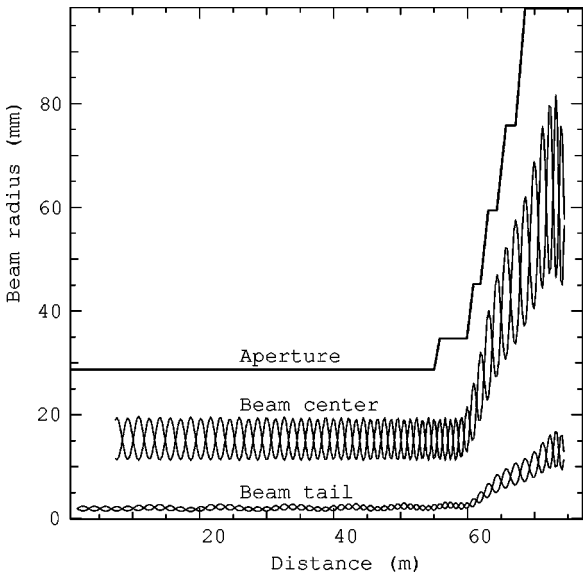

FIG. 2. The horizontal and vertical beam semi-axes, as well as the aperture, as a function of position along the drift compression section.

The final beam pulse will therefore be different from the desired final beam pulse. The difference is typically negligible,[10] since the beam radii in the forward and backward run are approximately equal on average even after rematching.

Generally, the drift compression section for heavy ion inertial fusion is designed such that the beam expands transversely near the end of drift compression in order to enable focusing the beam onto a small spot. In the example drift compression system shown here, the beam expands smoothly from 1.5 cm at the beginning of drift compression to 6 cm at the end. The aperture was chosen to increase in finite steps. This drastically reduces the run time of a comparative 3D particle-in-cell simulation of the system, since the capacity matrix to calculate the image charges on the pipe needs to be recalculated only a few times.

A drift compression section was designed for a K^+ ion beam of 3.90625 μC at an energy of 200 MeV, which are typical IRE parameters. The final beam duration was chosen to be 3 ns, while the final beam profile consisted of a flat-top with 25% parabolic ends on each side. The beam was divided into 400 slices longitudinally, each slice having the same amount of charge. The longitudinal electric field was calculated on a 64×512 (r, z) grid. A time step size was used that corresponds to a distance traveled by the beam of about 5 mm.

Figure 2 shows the horizontal and vertical semi-axes of the beam along the drift compression section both for the beam center and for the tail of the beam (defined as the leftmost slice boundary in the simulation). Whereas virtually no mismatch occurs at the beam center, near the end of drift compression a small mismatch develops at the tail, where the beam current increases most rapidly. A similar mismatch occurs for the head of the beam.

The position of the slice boundaries at the end of drift compression is shown in Fig. 3 as a function of the slice index. On a global scale, this curve seems to be very smooth.

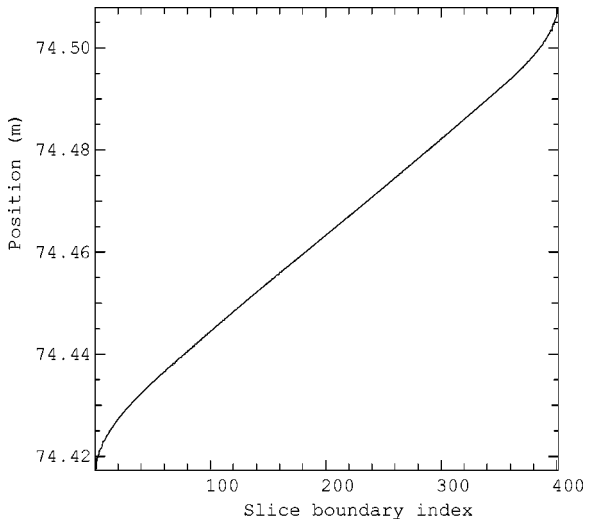

FIG. 3. The position of the slice boundaries as a function of their index at the end of the drift compression section. Even though the curve appears to be very smooth and monotonically increasing, this figure contains nine slice overtaking events.

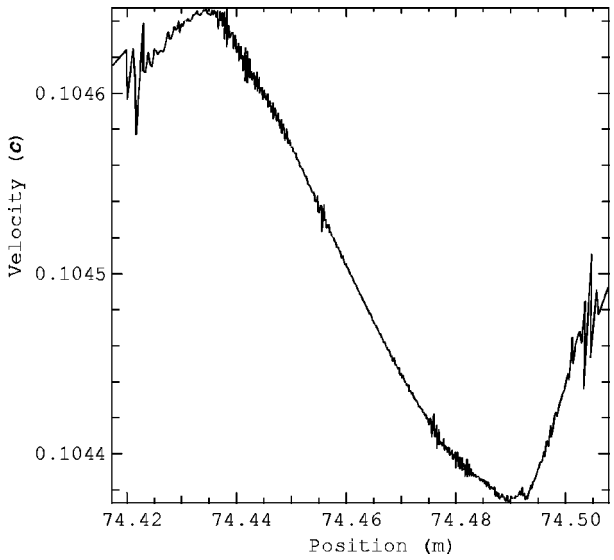

FIG. 5. The longitudinal phase space of the beam at the end of the drift compression section.

However, there were nine occurrences of slice overtaking in this beam. An example of slice overtaking occurring near the beam center is shown in Fig. 4. This illustrates that slice overtaking should not be regarded as a major deviation of the behavior of the beam. Rather, slice overtaking suggests the occurrence of longitudinal mixing on a local scale.

The longitudinal phase space is shown in Fig. 5. Near the beam ends, an increase in the longitudinal emittance is manifested by a larger area of phase space occupied by the beam. The emittance growth can be understood in more detail by performing 1D (longitudinal), 2D (r, z), or 3D particle-in-cell simulations of the beam. Globally, the phase space area occupied by the beam is still well represented by a smooth curve, which validates the applicability of the cold phase space model in this regime.

Figure 6 shows the longitudinal phase space of a section of the beam in which slice overtaking occurred (compare to Fig. 4). The longitudinal velocity has become double valued as a consequence of slice overtaking. This would cause a conventional fluid model to break down.

V. DISCUSSION

The longitudinal dynamics of a charged particle beam can be simulated by dividing the beam into slices longitudinally and calculating the longitudinal motion of the slice boundaries. Previously, the beam was then treated as a 1D fluid, in which slices retained their order, and slice overtaking was considered to be caused by an insufficiently accurate simulation. In addition, a slice compressed to zero width would have an infinite line charge density, resulting in an

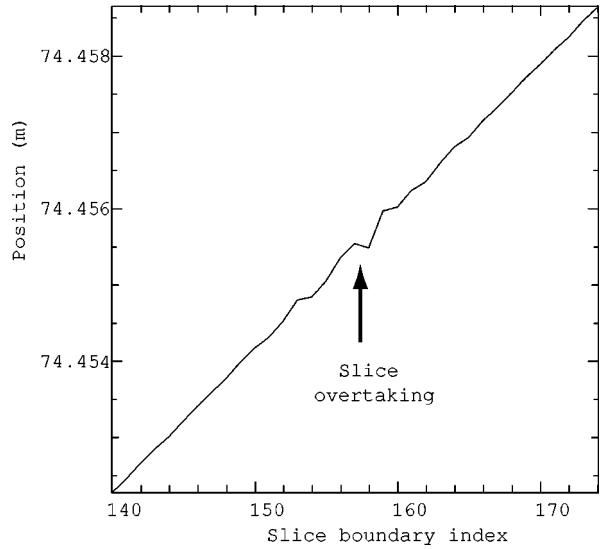

FIG. 4. The position of the slice boundaries of a short section of the beam as a function of their index at the end of the drift compression section, showing an example of slice overtaking.

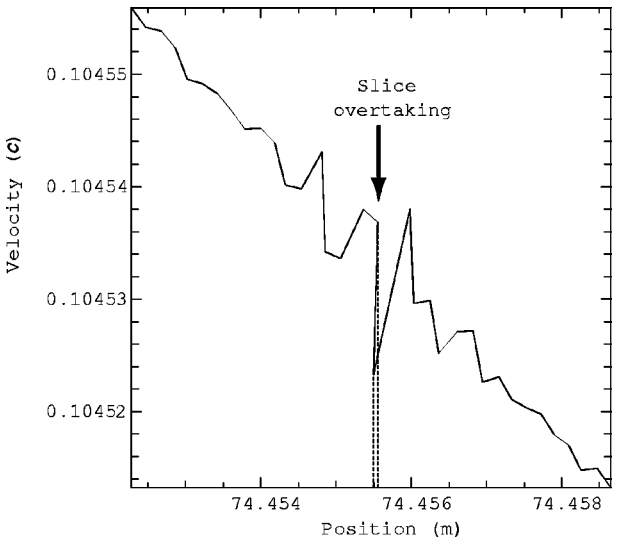

FIG. 6. The longitudinal phase space of a section of the beam at the end of the drift compression section, showing that the longitudinal velocity has become double valued due to slice overtaking.

infinite current in the transverse envelope equation. In practice, simulations were therefore stopped as soon as two slices overtook each other.

However, the repulsive force on a slice boundary being bounded as a slice is compressed to zero width implies that this model intrinsically, though implicitly, includes slice overtaking. A simple fluid model is therefore unsuitable to describe the longitudinal dynamics of a beam and should be replaced by a cold phase fluid model. An infinite line charge density can then be avoided by averaging the charge density over a small longitudinal distance.

In simulations of our cold phase fluid model, slice overtaking occurred regularly without disturbing the overall dynamics of the beam. Slice overtaking may be caused by the numerics as well as by the physics of the problem. Whereas slice overtaking events are expected to occur near the beam ends, where the longitudinal field varies rapidly, numerics may be the cause of slice overtaking in the beam core. However, even then a cold phase fluid model is preferable over a simple fluid model, as it allows us to perform a sequence of simulations of increasing accuracy. In a converged simulation either slices do not overtake each other, or the few remaining slice overtaking events do not appreciably affect the calculation of the physical quantities in which we are interested. A simple fluid model does not allow us to perform such a sequence of simulations, since numerous simulations would have to be halted prematurely due to slice overtaking. In addition, increasing the number of slices to improve the accuracy of a simulation leads to a closer distance between the slice boundaries, making slice overtaking more likely. Therefore, even very accurate simulations with a large number of slices may break down if a simple fluid model is used.

Slice overtaking caused by the physics of the problem is indicative of local longitudinal mixing of the beam. Rapidly expanding ends of a highly compressed beam, or imperfect matching as in the example we showed, may lead to local mixing and therefore to slice overtaking in the cold phase fluid model. In addition, to investigate the effect on drift compression of errors in the initial longitudinal velocity gradient, a random longitudinal velocity error may be added to the slice boundaries initially. This may lead to slice overtaking at an early stage of the simulation.

In the case of extreme slice overtaking, the resulting phase space structure can be seen as representing the thermal spread in the longitudinal velocity. Additional calculations using particle-in-cell simulations would be necessary to understand such a phase space structure fully.

We can compare our results to the case of a high-brightness electron beam, in which the beam length may be much shorter than the pipe radius. The presence of the conducting wall can then be ignored and a free-space solution can be employed. An example of longitudinal bunching of an electron beam[12] using a particle-in-cell calculation shows how the longitudinal phase space folds over, resulting in longitudinal mixing on a global scale. In the regime relevant to heavy ion fusion, however, the beam is much longer than the pipe radius at the beginning of drift compression, and comparable to the pipe radius at the end. A free-space solution would therefore not be suitable. Although we were able to avoid global mixing by a careful design of the drift compression system, the cold phase-space model showed that mixing on a local scale does occur.

ACKNOWLEDGMENTS

The authors wish to thank W. M. Sharp for useful discussions on the fluid model.

This work was performed under the auspices of the U.S. Department of Energy under University of California Contracts No. DE-AC03-76SF00098 at LBNL, and No. W-7405-ENG-48 at LLNL.

APPENDIX: CALCULATION OF BESSEL SUMS

The Kneser–Sommerfeld formula for a Bessel function of order zero is given by[13,14]

$$\sum_{n=1}^{\infty} \frac{J_0(x_n\alpha)J_0(x_n\alpha')}{(s^2-x_n^2)[J_1(x_n)]^2} = \frac{\pi J_0(\alpha s)}{4J_0(s)}[J_0(s)Y_0(\alpha' s)-Y_0(s)J_0(\alpha' s)], \tag{A1}$$

for $0\leqslant\alpha\leqslant\alpha'\leqslant 1$. This formula can be derived using Cauchy's residue theorem. A different version of the Kneser–Sommerfeld formula given in the classic text on Bessel functions by Watson[15] is incorrect.[16–19]

By taking the derivative with respect to s of both sides of this equation, and evaluating the result at $s=0$, we find

$$\sum_{n=1}^{\infty} \frac{J_0(x_n\alpha)J_0(x_n\alpha')}{x_n^4[J_1(x_n)]^2} = \frac{1}{8}[(\alpha^2+\alpha'^2)\ln\alpha+\alpha^2-1]. \tag{A2}$$

Next, we take the derivative with respect to α' to find

$$\sum_{n=1}^{\infty} \frac{J_0(x_n\alpha)J_1(x_n\alpha')}{x_n^3[J_1(x_n)]^2} = -\frac{1}{4}\alpha'\ln\alpha. \tag{A3}$$

For $\alpha=\alpha'$, this reduces to the Bessel sum appearing in Eq. (12). By taking the derivative with respect to α, we find

$$\sum_{n=1}^{\infty} \frac{J_1(x_n\alpha)J_1(x_n\alpha')}{[x_nJ_1(x_n)]^2} = \frac{1}{4}\frac{\alpha'}{\alpha}, \tag{A4}$$

which for $\alpha=\alpha'$ reduces to the Bessel sum used to derive Eq. (16).

Alternatively, Eqs. (A3), (A4) can be derived by setting the radial electric field of an infinitely long cylindrical beam with radius a equal to the radial electric field calculated from the electrostatic potential given in Eq. (9).

[1] W. M. Sharp, J. J. Barnard, D. P. Grote, S. M. Lund, and S. S. Yu, *Proceedings of the 1993 Computational Accelerator Physics Conference*, 22–26 February 1993, Pleasanton, California, AIP Conf. Proc. 297, edited by R. Ryne (American Institute of Physics, New York, 1993), pp. 540–548.
[2] A. Hofmann, CERN 77-13, 1977, p. 139.
[3] W. M. Sharp, A. Friedman, and D. P. Grote, Fusion Eng. Design **32–33**, 201 (1996).
[4] W. M. Sharp (private communication, 2001).
[5] W. M. Sharp, D. A. Callahan, A. Friedman, and D. P. Grote, *Proceedings of the 1996 Computational Accelerator Physics Conference*, 24–27 September 1996, Williamsburg, Virginia, AIP Conf. Proc. **391**, edited by J. J.

Bisognano and A. A. Mondelli (American Institute of Physics, Woodbury, NY, 1997), pp. 27–38.
[6]J. D. Jackson, in *Classical Electrodynamics* (Wiley, New York, 1975), p. 106.
[7]A. Friedman, D. P. Grote, and I. Haber, Phys. Fluids B **4**, 2203 (1992).
[8]R. D. Richtmyer and K. W. Morton, in *Difference Methods for Initial-Value Problems* (Wiley, New York, 1967), Chap. 12.
[9]F. H. Shu, in *The Physics of Astrophysics, Volume II: Gas Dynamics* (University Science Books, Sausalito, CA, 1992), Chap. 15.
[10]M. J. L. de Hoon, Ph.D. thesis, University of California, Berkeley, 2001.
[11]J. J. Barnard, L. E. Ahle, R. O. Bangerter, F. M. Bieniosek, C. M. Celata, A. Faltens, A. Friedman, D. P. Grote, I. Haber, E. Henestroza, R. A. Kishek, M. J. L. de Hoon, V. P. Karpenko, J. W. Kwan, E. P. Lee, B. G. Logan, S. M. Lund, W. R. Meier, A. W. Molvik, T. C. Sangster, P. A. Seidl, and W. M. Sharp, Nucl. Instrum. Methods Phys. Res. A **464**, 621 (2001).
[12]L. Serafini and M. Ferrario, *Proceedings of the 19th ICFA Beam Dynamics Workshop on X-Ray Free Electron Lasers and Their Applications*, 11–15 September 2000, Arcidosso, Italy, AIP Conf. Proc. 581, edited by S. Chattopadhyay (American Institute of Physics, Melville, NY, 2001), pp. 87–106.
[13]A. Kneser, Math. Ann. **63**, 477 (1907).
[14]A. J. W. Sommerfeld, Jahresber. Dtsch. Math.-Ver. **XXI**, 309 (1912).
[15]G. N. Watson, in *A Treatise on the Theory of Bessel Functions* (Cambridge University Press, Cambridge, UK, 1980), p. 499.
[16]H. Buchholz, Z. Angew. Math. Mech. **25/27**, 245 (1947).
[17]H. Hayashi, J. Phys. Soc. Jpn. **50**, 1391 (1981).
[18]H. Hayashi, J. Phys. Soc. Jpn. **51**, 1324 (1982).
[19]V. G. Vaccaro and L. Verolino, Nuovo Cimento Soc. Ital. Fis., B **113**, 1527 (1998).